Charm, the Virtual Photon and the Micro Vertex Detector

Matthew S. Lightwood

02. July 2001

Abstract:

The clock and control electronics of the micro vertex detector recently installed in ZEUS are described, and the future role of the detector in heavy flavour physics is briefly discussed. The dependence of the virtual photon structure on its virtuality, Q^2, is studied for the first time in events containing dijets and a charm particle with the ZEUS detector at HERA using an integrated luminosity of 104 pb^{-1}. The measurement is made in the kinematic range $Q^2 < 5.10^3 \mathrm{GeV}^2$ using dijet events containing a $D^{*\pm}$. Events having two jets with large transverse energies are selected using the longitudinally invariant k_T algorithm in the laboratory frame. The dijet cross section is measured as a function of the fractional momentum of the photon participating in the dijet production, (x_γ^{OBS}), and of Q^2. The ratio of the cross section at low x_γ^{OBS} ("resolved photon") relative to high x_γ^{OBS} ("direct photon") is compared to the predictions of leading-order pQCD.

1 Introduction

This year has seen a shut down for the HERA ep collider and the ZEUS detector in Hamburg, Germany. During this time numerous upgrades have been carried out to the HERA ring, and the ZEUS detector has been enhanced by the installation of a new microvertex detector (MVD) and straw tube tracker(STT). Although this has meant a cessation of data acquisition over this period, the year has been far from quiet. UCL have taken a leading role in the design and implementation of the electronics used to drive the MVD, as well as continuing the exploration of high energy physics using data from previous years. An overview is given of my contribution to the MVD, and the result of an analysis of dijet cross sections associated with charm is presented.

2 The ZEUS Detector At HERA

The HERA accelerator at DESY in Hamburg is the world's only ep collider. Measuring 6.3km in circumference the accelerator allows us the unique oportunity to study the high energy interactions between electrons (or positrons) of 30Gev and protons of 920Gev. The layout of the accelerator and the pre-acceleration ring, PETRA, are shown in figure 1.

The ZEUS detector is one of two multipurpose HERA experiments and is situated at one of the four interaction points on the ring. A schematic diagram of the detector is shown in figure 2. Immediately around the beam pipe is the microvertex detector, a double sided silicon strip detector used to observe the vertex at which scattered particles decay. The barrel part of the detector is 60 centimetres long with silicon sensors arranged in layers around the beam pipe. The forward part consists of four circular shaped discs, again with silicon sensors distributed over their surfaces. This new detector has replaced the old vertex detector and will increase the intrinsic resolution for normal incident tracks from between 50-150μm to an expected value of 10μm. Surrounding this is the central tracking detector (CTD). The CTD consists of 72 cylindrical drift chamber layers organised into 9 'super layers' each with 8 sense wires. The CTD gives a spatial resolution of approximately 260μm, and a resolution in the transverse momentum of $\sigma/\mathrm{p}_t = 0.002\ \mathrm{p}_t \oplus 0.003$ in Gev/c. In the coming years these two detectors will be used together to measure the interaction vertex with unparrelled accuracy in ep collisions.

Energy measurements contribute a great deal to our ability to understand the observed interactions. The important job of accurately measuring the energy deposited in the detector is given over to the high resolution uranium calorimeter(CAL). The calorimeter consists of plates of depleted uranium seperated by plastic scintillator, giving us the best possible energy resolution for observing hadrons. The CAL is further split into three parts, the forward calorimeter (FCAL), the barrel calorimeter(BCAL) and the rear calorimeter (RCAL). The output from the CAL is read out through photomultiplier tubes. Outside of the central detectors is the veto wall, which consists of two planes of orthogonal scintillator strips. The veto wall is used for tagging particles from beam gas interactions.

3 The Microvertex Detector and Electronics

With the increased luminosity of HERA following this years upgrade the emphasis in the coming years will be to study effects at even higher E_t. It is hoped that the MVD will allow us sufficient improvement in momentum and position resolution to allow the reconstruction of secondary vertices. The installation will allow us to identify particles, in particular those containing heavy flavors, with minimal background, an important development if we are to improve on the measurements presented in section 4. With this in mind the design goals were set out as follows.

- Polar angle coverage between 10° - 170°

- Three spatial measurements per track, in two projections.
- 20 μm intrinsic hit resolution for normal incident tracks.
- Impact parameter resolution of 100μm for polar angle of 90 degrees, increasing gradually to 1mm at 20°. (For Track p > 2Gev).
- Noise occupancy $< 10^{-3}$.
- Hit efficiency > 97%.
- Alignment accuracy 20μm.
- Two Track seperation 200μm.

During this project UCL has been actively involved in the design production and implementation of the clock and control electronics. HELIX is the front end chip of which there are 2048 situated within the detector. The clock and control hardware provides an interface between the ZEUS global first level trigger (GFLT), the run control system, the analogue to digital converter (ADC) crates and the HELIX readout chips, see figure 3. Installing these HELIX drivers and the myriad of associated cabling was one of my tasks over the complete installation period of the MVD.

The 'work' of the 16 helix drivers is done within a programable logic device (PLD) situated on each of the boards. The PLD is an ideal device for use on this project, as it allows us the chance to modify the opperation of the board during and after testing, an option ruled out by 'hard wired' systems. The best way to understand how the PLD works is to imagine it as a series of blocks each containing a series of logic gates with a large number of conections to one another. These conections can be programmed open or closed - creating a useful logic system. Because the PLD is programable the number of operations we can perform on a single chip is only limited by it's size. In other words it allows us to carry out multiple tasks on a single device, a great advantage both in speed as well as footprint in an area where space is at a premium.

Each of the HELIX drivers fan out to 16 read out cells, each cell consisting of 8 HELIX chips, giving a total of 256 readout cells on the detector. These are conected by a series of 144 twisted pair cables on each board, representing a major organisational challenge for the joint UCL/Oxford team, of which I was a member, whose responsibility it was to lay and test the clock and control cabling. The functionality of the PLD's was decided by a team of engineers from UCL and finally programmed by Matthew Warren. Because of the complexity of the device, and the need for them to work precisely the boards were prepared in three stages. Firstly a wire wrap of the design was produced to test the concept. This was followed by the production of eight (half the final total) printed circuit boards (PCB) at RAL, which were used for the initial tests in hamburg, and helped us to develop the design to optimise performance. The final product was installed in june 2001 following succesful system tests.

Because of the speed with which the boards operate their consistancy had to be tested over a large number of triggers. Each element of the PLD can be accessed by address through the back of the VME crate. I used this fact to create a peice of test software which generated a random number (or pseudorandom) and passed this through each register and compared the desired output with the actual output and scanned for anomalies. The software helped us gain a handle, not only on if a problem existed, but also precisely where it was to be found. This was crucial in both the initial development of the boards as well as the system tests in Hamburg. The fact that the boards could be accessed through the back of the VME crate meant that it was not necessary to unplug the cabling to test the boards when problems were suspected during these tests.

The current status of the MVD is promising. It has now been fully tested with cosmic ray events and installed into the ZEUS detector ready for the first run of the upgraded HERA accelerator. Much work is still to be done in trying to understand the detector and how it performs under run conditions. This work will in no small part be contributed to by UCL over the coming years, and will greatly improve the quality of results extracted from the ZEUS detector.

4 Virtual Photons with Charm.

Earlier this year an analysis by UCL's Ben West, suggested that interesting physics existed when we demand charm in the virtual photon. It appeared that a surpression existed which was not fully understood by existing models. In order to validate the result it was important that we performed an independent second analysis of the results before they could be formally presented. I carried out this task over the same data sample using Orange and ROOT, in contrast to Ben's original analysis carried out in PAW.

Studies of jet photoproduction at HERA [?] and photon-photon processes at LEP [?] have established that the real photon, in addition to its point-like couplings to charged quarks and leptons, also has a partonic structure. This structure is resolved by the hard scale present in such processes. The dependence of this partonic structure on the photon's virtuality, Q^2, has also been studied . These studies have shown that measurements may be interpreted in terms of partonic structure that is suppressed as Q^2 increases. It has also been shown that requiring the presence of charm in the final state of jet photoproduction processes suppresses the partonic structure of the photon . The question of whether these two phenomena - suppression in the presence of a non-zero virtuality and suppression in the presence of charm - share a common physical mechanism, is a natural and important one to ask for the understanding of heavy flavour production in a hadronic environment. It is this question that is addressed in this paper. The evolution of the virtual photon structure for $Q^2 < 5 \cdot 10^3$ GeV^2 is measured for the first time using dijet events which contain a $D^{*\pm}$ meson in ep scattering at HERA. GeV2

In leading-order (LO) perturbative QCD (pQCD) two components contribute to jet photoproduction processes at HERA. In direct photon processes the entire momentum of the photon takes part in the hard subprocess with a parton from the proton, whereas in resolved photon processes, the photon acts as a source of partons, and one of these, carrying a fraction of the photon's momentum, enters the hard subprocess. Both LO processes have two outgoing partons of large transverse energy, resulting in dijets in the final state. In resolved photon processes, the photon structure is commonly described via parton distribution functions (PDFs) which receive contributions from both perturbative and non-perturbative terms.

As the photon virtuality becomes non-zero, the non-perturbative contributions to the photon PDFs are expected to diminish. In this region, the language of photon PDFs may still be retained in describing processes where the photon splits into a $q\bar{q}$ pair before interacting with the proton; however, the photon PDFs are here in principle calculable in pQCD. QCD predicts that for $(E_T^{jet})^2 >> Q^2$, the virtual photon PDFs should decrease logarithmically as Q^2 grows, until $Q^2 = (E_T^{jet})^2$, at which point only the direct contribution should remain.

In charm processes, involving real or virtual photons, the charm mass provides a hard scale in additiona to that provided by the high transverse energy jets. This is also expected to suppress the relative contribution of resolved processes, since the generation of any charm "content" for the photon requires higher virtuality fluctuations and will be subject to threshold effects not present for lighter quarks. In a previous measurement it was found that in LO MC models, the charm in dijet resolved photon events was mostly attributed to charm excitation. A detailed study of the dynamics of the production mechanism in these process is the subject of another submission [**?**].

This paper presents the ratio of the measured dijet cross sections for $x_\gamma^{\mathrm{OBS}} < 0.75$ and $x_\gamma^{\mathrm{OBS}} > 0.75$ as a function of Q^2 for events containing a $D^{*\pm}$. The values of the cross section ratio are compared with predictions of pQCD for the cross section ratio with and without this $D^{*\pm}$ requirement.

5 Experimental setup

The analysis was performed with the data taken by the ZEUS collaboration from 1996 to 2000. In 1996-1997 HERA collided positrons with energy $E_e = 27.52$ GeV and protons with energy $E_p = 820$ GeV ($820e^+$). In 1998-1999 HERA collided electrons with energy $E_e = 27.52$ GeV and protons with energy $E_p = 920$ GeV ($920e^-$). In 1999-2000 HERA collided positrons with energy $E_e = 27.52$ GeV and protons with energy $E_p = 920$ GeV ($920e^+$). The integrated luminosity used in this analysis is 104 pb^{-1}.

A detailed description of the ZEUS detector can be found elsewhere [?]. A brief outline of the components which are most relevant for this analysis is given below.

The high-resolution uranium–scintillator calorimeter (CAL) [?] consists of three parts: the forward (FCAL), the barrel (BCAL) and the rear (RCAL) calorimeters. Each part is subdivided transversely into towers and longitudinally into one electromagnetic section (EMC) and either one (in RCAL) or two (in BCAL and FCAL) hadronic sections (HAC). The smallest subdivision of the calorimeter is called a cell. The CAL energy resolutions, as measured under test beam conditions, are $\sigma(E)/E = 0.18\sqrt{E}$ for electrons and $\sigma(E)/E = 0.35\sqrt{E}$ for hadrons (E in GeV).

Charged particles are tracked in the central tracking detector (CTD) [?], which operates in a magnetic field of 1.43 T provided by a thin superconducting coil. The CTD consists of 72 cylindrical drift chamber layers, organized in 9 superlayers covering the polar angle

region $15^\circ < \theta < 164^\circ$. The transverse-momentum resolution for full-length tracks is $\sigma(p_T)/p_T = 0.0058 p_T \oplus 0.0065 \oplus 0.0014/p_T$, with p_T in GeV.

6 Kinematics

The kinematics of the reaction

$$e^+(k) + p(P) \to e^+(k') + jet + jet + X$$

are described in terms of $Q^2 = q^2 = (k - k')^2$ and the fractional energy transferred to the proton in its rest frame $y = (k - k') \cdot P/(k \cdot P)$. Experimentally, y and Q^2 were reconstructed from the measured energy, E'_e, and polar angle[1],

[1]The ZEUS coordinate system is a right-handed Cartesian system, with the Z axis pointing in the proton beam direction, referred to as "forward direction", and the X

θ_e, of the scattered electron as:

$$Q^2 = 2E_e E'_e(1 + cos\theta_e)$$

$$y = 1 - \frac{E'_e}{2E_e}(1 - cos\theta_e).$$

The variable $y_{\rm JB} = \Sigma_i(1 - \cos\theta_i)/(2E_e)$, where the sum runs over all CAL cells except those assigned to the scattered electron candidate, also gives a measurement of y .

For events with two jets in the final state, resolved and direct photon processes are separated experimentally via the variable $x_\gamma^{\rm OBS}$, defined as:

$$x_\gamma^{\rm OBS} = \frac{\Sigma_{jets} E_T^{jet} e^{-\eta^{jet}}}{2yE_e}$$

where E_T^{jet} is the jet transverse energy, and $\eta^{jet} = \ln(\tan(\theta_{jet}/2))$ the jet pseudorapidity (θ_{jet} being the jet polar angle). At $x_\gamma^{\rm OBS} \geq 0.75$, the direct component dominates , while the $x_\gamma^{\rm OBS} < 0.75$ region is sensitive mainly to the resolved component. However, events with low values of $x_\gamma^{\rm OBS}$ can also be produced when initial- and final-state parton showers give rise to hadronic activity outside the dijet system. In pQCD, $x_\gamma^{\rm OBS}$ is well defined at all orders, and thus measurements based on it can be compared with theoretical predictions at any given order.

7 Data selection

The events were selected online via a three-level trigger system using the same trigger selection algorithms as in a previous dijet publication , except that in the third level trigger (TLT) the transverse energy requirement was raised to $E_T^{TLT} > 4.5$ GeV for the $920e^+$ running period. The sample was separated offline into subsamples corresponding to two different Q^2 ranges:

- Photoproduction (PHP) events were selected by requiring that no identified electron was found in the CAL with energy $E'_e > 5$ GeV and $y < 0.7$. The resulting sample had $Q^2 < 1.0$ GeV^2 with an estimated median of 10^{-3} GeV^2;

axis pointing left towards the centre of HERA. The coordinate origin is at the nominal interaction point.

- Deep inelastic scattering (DIS) events were selected by requiring that the outgoing electron was measured in the CAL. The energy of the scattered electron was required to satisfy $E_e^{'} > 10.0$ GeV.

For both samples additional cuts of $0.15 < y_{\rm JB} < 0.55$ were applied. Due to the energy lost in the inactive material in front of the CAL, and to particles lost in the rear beampipe, $y_{\rm JB}$ systematically underestimates the true y by approximately 10-20%, an effect which is adequately reproduced in the Monte Carlo simulation of the detector. The combination of y_{JB} and $E_e^{'}$ cuts ensured that the two samples correspond to the same true y range $(0.2 < y < 0.65)$.

The longitudinally invariant k_T algorithm in the inclusive mode was then applied to the CAL cells to search for events with two jets in the final state. The cells assigned to the scattered electron candidate were excluded from the jet search for events in the DIS sample. The two jets with the highest transverse energy in the pseudorapidity range $|\eta^{jet}| < 2.4$ were required to have transverse energies $E_T^{jet} > 4.0$ GeV. After correction for energy lost in the inactive material in front of the CAL this approximates the kinematic region $E_{T,1}^{jet} > 7.5$ GeV and $E_{T,2}^{jet} > 6.5$ GeV, where the measurement is made.

Long charged tracks measured by the CTD and assigned to the primary event vertex are selected and analysed as follows. All pairs of tracks are analysed and assigned to be either of type "kaon" or of type "pion". All the combinations of tracks with opposite charge and $p_T(K,\pi) > 0.45$ GeV are combined and kept if their mass is in the range $1.8 < m(D^0) < 1.92$ GeV. These pairs of tracks are then combined with a track of type "pion", called the *slow pion*, π_s due to its low energy, which has the opposite charge to the track of type "kaon" and, $p_T(\pi_s) > 0.15$ GeV. This combination of three tracks then forms a $D^{*\pm}$ candidate which is accepted if $p_T(D^{*\pm}) > 3$ GeV and $|\eta(D^{*\pm})| < 1.5$.

Figure 4 shows the mass difference, $\Delta M = m(D^{*\pm}) - m(D^0)$, distribution for the $D^{*\pm}$ candidates in the restricted Q^2 and $x_\gamma^{\rm OBS}$ regions of this analysis. The number of candidates was determined from an unbinned fit to the ΔM distribution using a Gaussian function to describe the $D^{*\pm}$ contribution, together with a term for the background:

$$F(\Delta M) = P1/(\sqrt{2\pi} \cdot \sigma(\Delta M)) \cdot exp(0.5 \cdot (\Delta M - <\Delta M>)^2/\sigma(\Delta M) + P2 \cdot (\Delta M - m_\pi)^{P3}$$

where $\sigma(\Delta M)$ and $<\Delta M>$ are the width and position of the Gaussian determined from a 5 parameter fit to the complete sample, m_π is the mass of the pion, and P1-P3 are free parameters. The fitted value $<\Delta M>$ was 145.51 ± 0.03(stat.), which should be compared with the present PDG value of 145.397±0.030. The fitted value of $\sigma(\Delta M)$ was 0.76±0.03 MeV, consistent with that anticipated from our resolution.

After all cuts and the jet search the estimated number of events with a $D^{*\pm}$ was 2200 ± 61 for the PHP sample and 421 ± 25 for the DIS sample.

8 Data corrections and systematics

The data were corrected for acceptance, smearing and kinematic cuts using the PYTHIA 6.1 [?] Monte Carlo (MC) model. Leading order resolved (LO-RES) and direct (LO-DIR) processes were generated separately. The SaS1D and MRSA sets were used for the photon and proton parton distribution functions (PDF), respectively. The MC events were processed through the full ZEUS detector simulation, based on the GEANT 3.13 program [?], using the same cuts as applied to the data. The normalisations of the LO-RES and LO-DIR processes were extracted from the data using a one-parameter fit to the uncorrected $x_\gamma^{\rm OBS}$ distributions. This procedure was applied separately for each Q^2 range.

The ratio of the low and high $x_\gamma^{\rm OBS}$ dijet cross sections , corrected to the hadron level, has been measured using the k_T jet algorithm. The measured cross section is for dijet events with a $D^{*\pm}$ in the phase space region defined by:

- $p_T(D^{*\pm}) > 3.0$ GeV; $|\eta(D^{*\pm})| < 1.5$;
- $E_T^{jet1,2} > 7.5,\ 6.5$ GeV; $|\eta^{jet}| < 2.4$;
- $0.2 < y < 0.65$;
- $Q^2 < 1.0$, $1.0 < Q^2 < 4.5$, $4.5 < Q^2 < 10.5$, $10.5 < Q^2 < 49.0$ and $49.0 < Q^2 < 5000.0$.

The cross sections at hadron level were obtained by multiplying the data distributions by a bin-by-bin correction factor, binned in two $x_\gamma^{\rm OBS}$ bins (0.00-0.75, 0.75-1.00). The correction factors take into account the efficiency of the trigger, the selection criteria, and the purity and efficiency of the jet and $D^{*\pm}$ reconstruction. The efficiency and purity were determined as a function of $x_\gamma^{\rm OBS}$ and Q^2 from the MC simulation. The purities lie between 0.3-0.65 and the correction factors lie between 1.0-1.6, except for $1.0 < Q^2 < 4.5$ GeV^2, where the correction factors lie between 3.0-3.6. In this region, where the impact point of the scattered electron in the CAL is close to the rear beam pipe, the acceptance for DIS events is lower.

A study of the systematic uncertainties of the measurements has been performed. The largest systematic uncertainty is due to the uncertainty of the CAL energy, $\pm 5\%$, which results in a systematic uncertainty of $\approx 10\%$ in the cross section ratio.

9 Results and discussion

The cross section ratio $R = \sigma(x_\gamma^{\rm OBS} < 0.75)/\sigma(x_\gamma^{\rm OBS} \geq 0.75)$ as a function of Q^2 is shown in Figure 5a. The cross section ratio is consistent with a constant. For comparison the predictions of HERWIG, where two options of the SaS1D virtual photon PDF are used, are also shown. One option implements a suppression of the partonic structure of the photon as a function of Q^2; in the other this suppression is turned off. The effect of the suppression is small and the data are not sufficiently accurate to distinguish between the models. In Figure 5b, the same data are compared to two models which implement no specific partonic structure for the photon, generating all low $x_\gamma^{\rm OBS}$ events from parton showers in two different schemes. The AROMA [?] model, which implements the DGLAP evolution scheme [?], lies below the data. The CASCADE model [?], which implements a version of the CCFM [?] evolution scheme, is much closer to the data.

The fact that the ratio does not change significantly with Q^2 in this range is in marked contrast to the case in which the charm requirement is not made, and suggests that the suppression of partonic structure due to charm and the suppression due to photon virtuality are not independent. To quantify this, the ratio should be compared to the previous results that did not require a $D^{*\pm}$ tag. Due to differences in the kinematic region, a direct comparison cannot be made. However, the SaS1D virtual photon PDF has been shown to describe the shape but not the normalisation of the ratio when no $D^{*\pm}$ is required[?]. The normalisation for $Q^2 < 1.0$ GeV^2 was measured in the kinematic region of this paper and found to be 70%. MC studies [?] show that $D^{*\pm}$'s from resolved events, which pass all other cuts of section 7, are more likely to fail the $\eta(D^{*\pm})$ and $p_T(D^{*\pm})$ cuts ; 20% for LO-DIR and 56% for LO-RES. Thus the $D^{*\pm}$ kinematic cuts are themselves a source of suppression of the resolved contribution. To estimate this, the effecr of correcting the ratio to the full $D^{*\pm}$ kinematic range using the HERWIG MC before is shown in Figure **??**. This extrapolation increases the ratio by a factor close to two, but does not strongly affect the shape.

The result of this extrapolation and the comparison to the "no charm required" case is shown in Figure **??**. This confirms quantitatively the qualitative conclusion drawn above. The partonic structure of the photon falls off much less rapidly in the presence of charm than it does when charm is not required. This demonstrates for the first time that the observed suppressions of partonic structure due to non-zero photon virtuality and due to charm are not independent.

10 Conclusion and Future Plans

In the previous academic year I feel I have been involved in a good cross section of projects. The first three months saw me take a key role in the testing and implementation of the HELIX driver boards, both at UCL and DESY in Hamburg. This role continued throughout the year and at every stage of development, from when the MVD was delivered, leading up to it's recent installation in the ZEUS hall. This work has given me a unique opportunity to gain some understanding of the hardware aspects of particle physics. This was followed by the second analysis described above, the results of which were presented by Ben West and made preliminary at the ZEUS collaboration meeting in June 2001. These results will now be presented formally at the EPS conference, Budapest, Hungary in mid July.

It is hoped in the coming year that I will continue to be involved in the commissioning of the MVD for physics. Of particular interest to me is the improvement the MVD, and indeed the HERA upgrade, will give in looking at heavy flavour physics, and a further analysis of photo production with charm is planned.

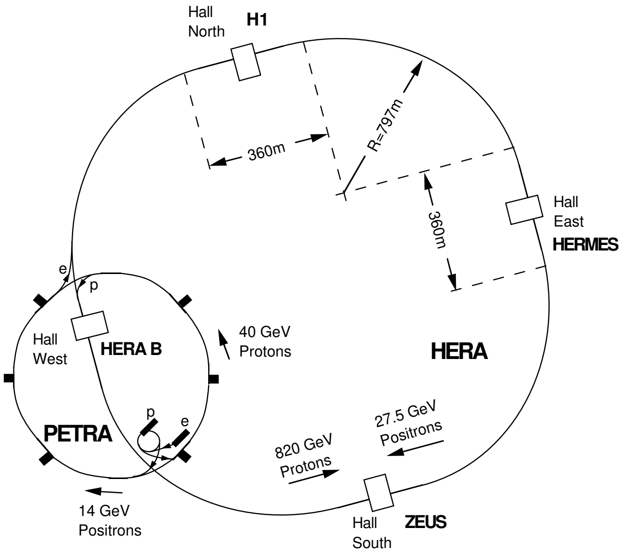

Figure 1: The HERA Accelerator, Hamburg, Germany.

Figure 2: The ZEUS detector.

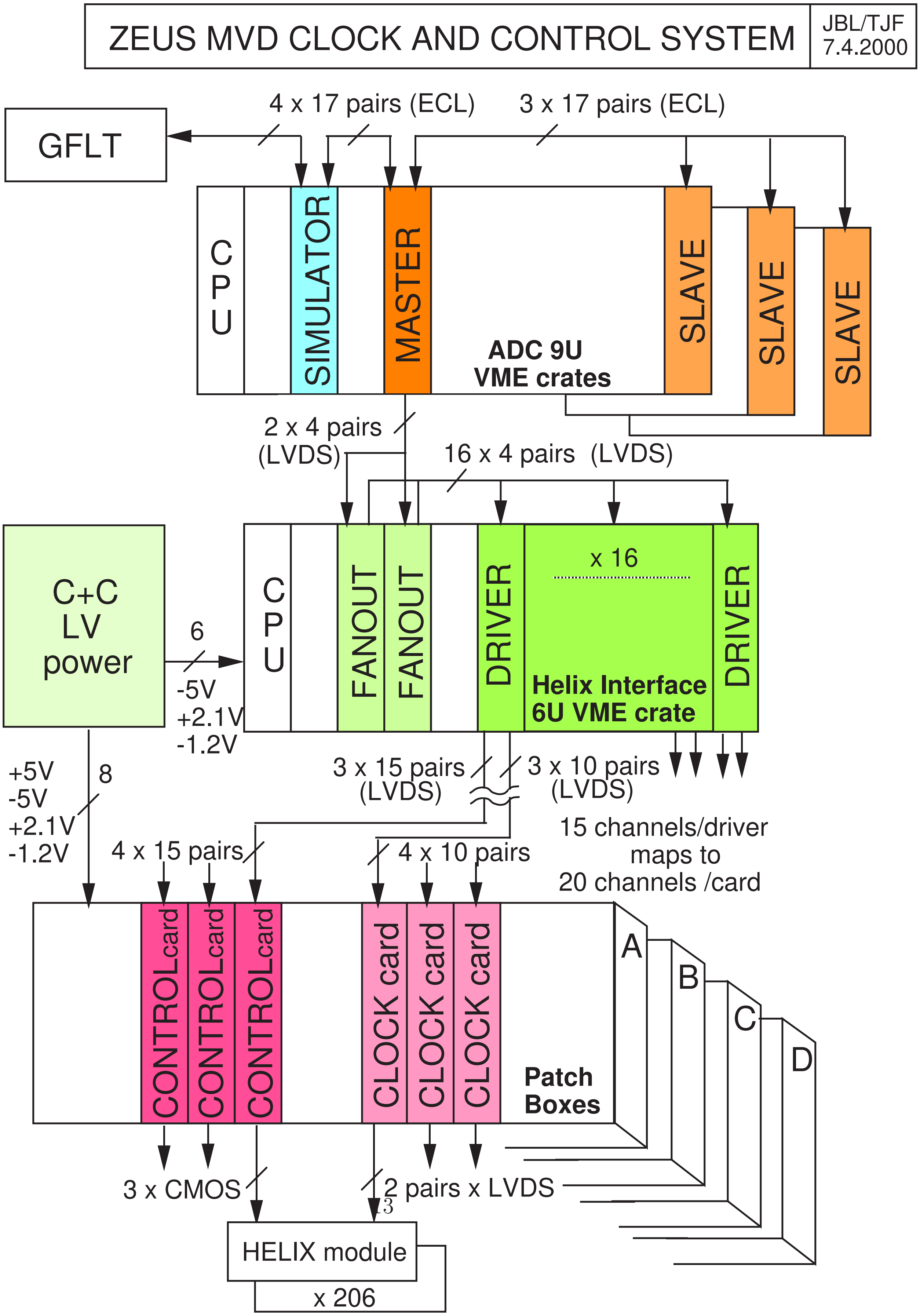

Figure 3: overall view of C+C hardware.

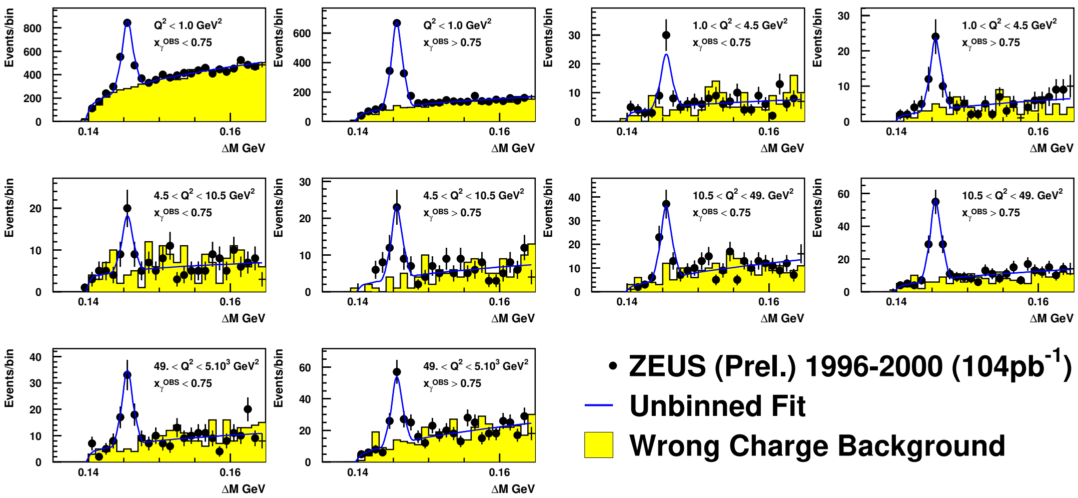

Figure 4: Signals for the 1996-2000 data, the line show the result of an unbinned fit to the signal and the histogram the wrong charge background estimate.

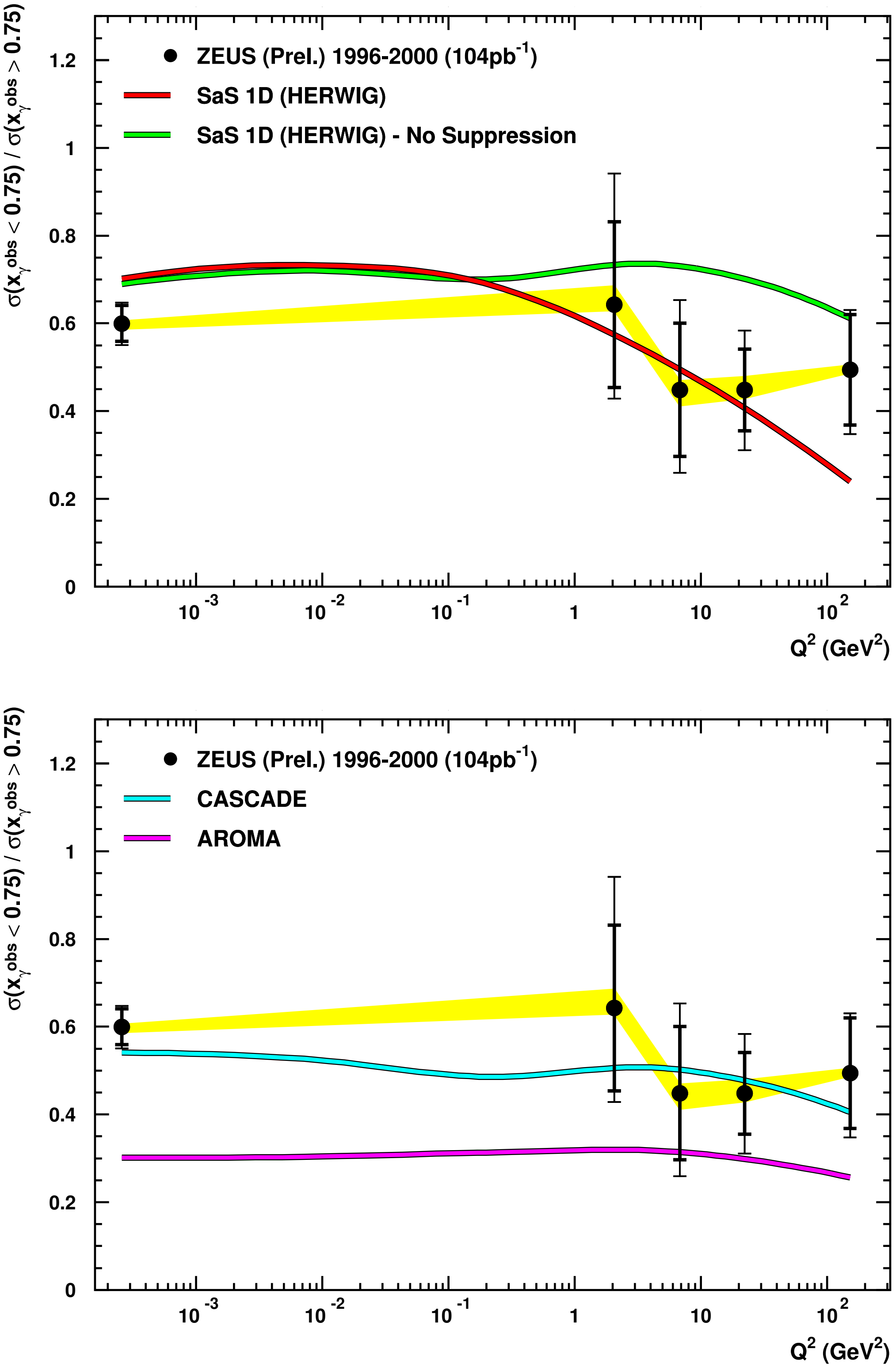

Figure 5: Ratio of low to high x_γ^{OBS} for events with a D^* compared to the predictions of the SaS1D photon structure function and the AROMA and CACSADE MCs which do not include photon structure.

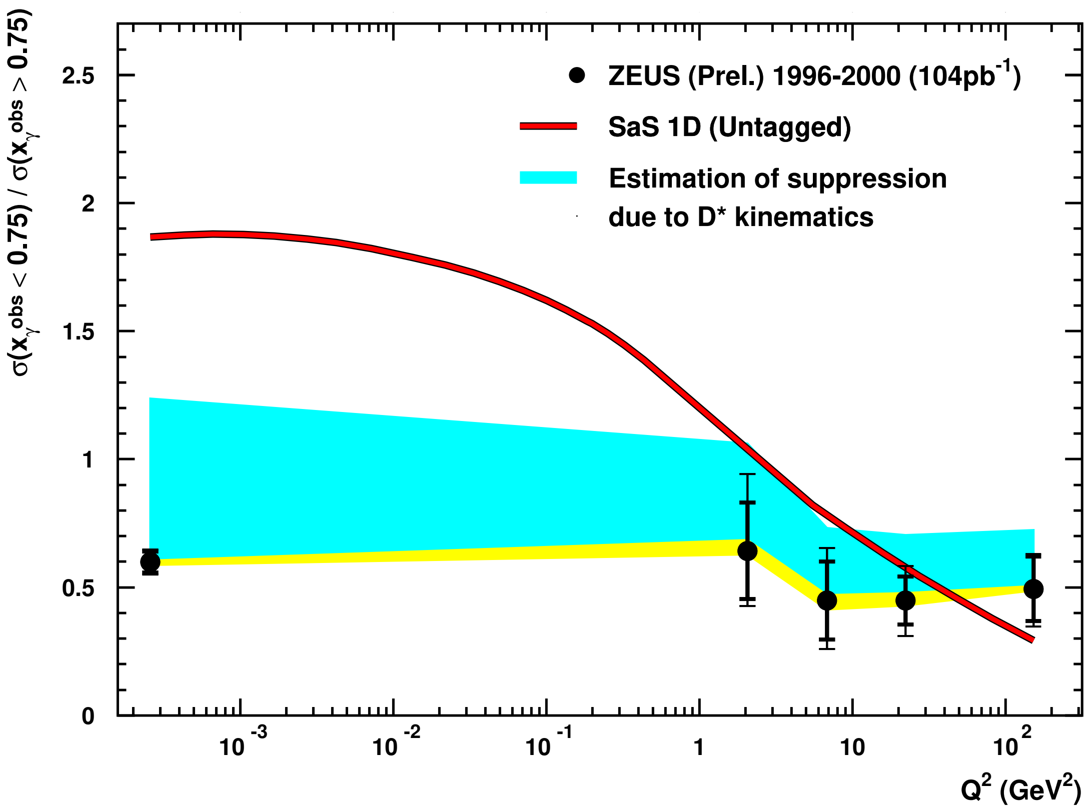

Figure 6: Corrected ratio of low to high $x_\gamma^{\rm OBS}$ for events with a D^* compared to the predictions of the SaS1D photon structure function for the ratio without a D^* tag.